Article

High Quality TaS$_2$ Nanosheet SPR Biosensors Improved Sensitivity and the Experimental Demonstration for the Detection of Hg^{2+}

Yue Jia [1], Yunlong Liao [2] and Houzhi Cai [1,*]

1   International Collaborative Laboratory of 2D Materials for Optoelectronic Science & Technology of Ministry of Education, Key Laboratory of Optoelectronic Devices and Systems of Ministry of Education and Guangdong Province, College of Physics and Optoelectronic Engineering, Shenzhen University, Shenzhen 518060, China; onlyjiayue@hotmail.com

2   International Collaborative Laboratory of 2D Materials for Optoelectronic Science & Technology of Ministry of Education, College of Optoelectronic Engineering, Shenzhen University, Shenzhen 518060, China; yl.liao@outlook.com

*   Correspondence: hzcai@szu.edu.cn

Abstract: TaS$_2$ as transition metal dichalcogenide (TMD) two-dimensional (2D) material has sufficient unstructured bonds and large inter-layer spacing, which highly supports transporting and absorbing mercury ions. The structural characterizations and simulation data show that an SPR sensor with high sensitivity can be obtained with a TaS$_2$ material-modified sensitive layer. In this paper, the role of TaS$_2$ nanoparticles in an SPR sensor was explored by simulation and experiment, and the TaS$_2$ layer in an SPR sensor was characterized by SEM, elemental mapping, XPS, and other methods. The application range of structured TaS$_2$ nanoparticles is explored, these TaS$_2$ based sensors were applied to detect Hg^{2+} ions at a detection limit approaching 1 pM, and an innovative idea for designing highly sensitive detection techniques is provided.

Keywords: TaS$_2$; nanoparticle; Hg^{2+}; sensor; SPR

1. Introduction

The concentration of heavy metal mercury ions (Hg^{2+}) in water is an important reference standard for people's health, and the maximum concentration of Hg^{2+} allowed in an effluent is 7.5 pM. Water contaminated with mercury ions (Hg^{2+}) and its detection is a global issue to be solved [1]. In the natural environment, Hg^{2+} exits in a stable state and might slowly accumulate in the food chain [2]. The existence of large amounts of Hg^{2+} may have a harmful effect on adult health and an even more harmful effect on the health of infants, foetuses, and lactating and pregnant women [3]. For instance, excess Hg^{2+} has a harmful effect on the digestive, immune, and nervous systems of an adult. It also causes severe harm to the stomach, lungs, and eyes of foetuses, and it may seriously damage them [4]. Hence, mercury pollution is considered a high risk to public safety and public health [5].

In order to lower the harmful effects produced as a result of mercury pollution, researchers have focused on limiting the release of substances that contain Hg^{2+} and have produced an extraordinarily low discharge standard [6,7]. For example, the US EPA standard is approximately 200pM [8], Japan's standard is 40 ng/g, and China's is 0.05 μg/L. However, current Hg^{2+} detection methods face numerous challenges as a result of the low discharge limit. The traditional technologies that detect Hg^{2+} are atomic fluorescence spectroscopy (AFS), electrochemistry (EC), and surface plasmon resonance (SPR) [9–16]. Thus, very sensitive pollution detection for Hg^{2+} is necessary [17,18]. The commonly used SPR optical sensing technologies have several advantages, for example, simple operation,

low cost, and good stability [19–21]. Recently, graphene and MoS_2 based SPR sensors were used as sensing layer materials [22–26]. However, due to the limited availability or shortage of sensing materials on gold surfaces, the use of old-fashioned SPR techniques for detecting low concentrations of metal ions is a big challenge. It is important to address the trace mercury ion low adsorption on to the current available sensing materials such as graphene, etc. [27,28]. Hence, recent research directions have focused on how to detect trace mercury ions and have illustrated the TaS_2-based SPR sensors sensing mechanism.

The two-dimensional (2D) TaS_2 material is currently a hot topic for researchers after the discovery of monolayer 1T-TaS_2 [29,30]. TaS_2 has a substantial potential for the removal of Hg^{2+}, which has made it a perfect candidate for Hg^{2+} sensing [31–35]. By selecting the TaS_2 material for a sensing layer as shown in Figure 1, a sensitive TaS_2-based SPR biosensor was successfully fabricated to detect Hg^{2+}, with TaS_2 nanosheets as the sensing layer. This novel SPR sensor is compatible with the demands of trace Hg^{2+} detection, and these TaS_2 based biosensors detection limit approaches 1 pM. It is evident from the results that the sufficient unsaturated bonds in the TaS_2 structure and large interlayer spacing-based biosensors promote adsorption of Hg^{2+} and efficient transport.
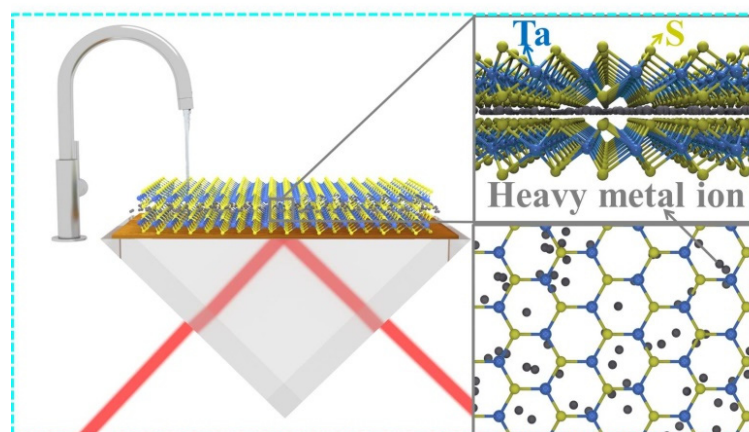

Figure 1. TaS2 nanoflakes as the sensing layer to detect trace mercury ions in SPR sensors.

2. Experiment

2.1. Synthesis of Superstructure TaS$_2$ Nanoflakes

The liquid phase stripping method was used to produce the 2D TaS_2 material ethanol suspensions. Using ultrasound and a mixture of purified water, the TaS_2 interlayer van der Waals force was overcome. Using a centrifuge, TaS_2 dispersions were formed by removing the TaS_2 block from single and multilayer TaS_2. First, 20 mg TaS_2 was dissolved in 20 mL water, and we treated the entire solution in bath sonication at a power up to 300 W for 10 h. Furthermore, we controlled the effective temperature of the bath sonication at approximately 10 °C. After the entire procedure, the acquired TaS_2 suspension was centrifuged for one hour with a rotation rate of 5000 r/min, then left for 12h for natural settling. For the upper layer liquid using a rotation rate of 12,000 r/min, the final step was centrifuged for 40 min. The subsequent supernatant was made of several layers of TaS_2 dispersion for use in the next experiments.

2.2. Assembling of TaS$_2$ Nanoflakes

TaS_2 nanoparticles accumulated on gold (Au) chips using a layer-by-layer technique. TaS_2 nanoparticle solution and polyetherimide (PEI) alternately flowed past the cell, and finally the TaS_2 layers were assembled by electrostatic adsorption. Surplus cations were washed by Milli-Q de-ionized water (18.2 MΩ cm) flowing past the cell. In each dipping period, the thickness increased, and the liquid current velocity was controlled to be lower than 1 mL/min to avoid separation of the finished films.

2.3. Mercury Ion Detection

Mercury ion in a water solution at concentrations from 10^{-12} M to 10^{-6} M as imitations of domestic water supply were prepared to systematically pass through SPR biosensor equipment. The buffer was domestic water. We washed the sample using ultra-pure water after immersing it in Hg^{2+} solutions for half an hour, and then spectrum signals were recorded. The detection signal was exported through a computer linked with a Kretschmann structure electrochemical in situ time resolved SPR sensor.

3. Results and Discussion

3.1. Numerical Simulation

The monolayer TaS_2 thickness is 0.361 nm [36,37]. The incident wavelength is 633 nm. In order to simulate this sensor sensitivity, the transmission matrix method is used. Type BK7 glass was selected as coupling prism, and 50 nm Au film was chosen as the metal layer. Equations for the BK7 glass refractive index was obtained from references [38,39]. The Au refractive index is represented by the Drude–Lorentz model [39]. The Au film surface was covered by TaS_2 to prevent Au from being oxidized in order to further enhance the sensibility of the designed sensors. The refractive index of TaS_2 is 12.25 + 3.06i [40–42]. The sensitive medium refractive index is expressed as n_s = 1.33 + Δn, whereas Δn designates the sensitive medium refractive index change caused by biological and chemical reaction.

The transfer matrix method was used [43] to calculate the N-layer model incident TM-polarized light reflectivity. These layers are piled vertically to the direction of the BK7 glass coupling prism for these TaS_2 allotrope sensors, and the name of each layer is selected using the dielectric constant (ε_k), thickness (d_k) and refractive index (n_k), separately.

$$\begin{bmatrix} U_1 \\ V_1 \end{bmatrix} = M \begin{bmatrix} U_{N-1} \\ V_{N-1} \end{bmatrix} \tag{1}$$

$$\prod_{K=2}^{N-1} M_K = \begin{bmatrix} M_{11} & M_{12} \\ M_{21} & M_{22} \end{bmatrix} \tag{2}$$

$$M_K = \begin{bmatrix} \cos \beta_K & \frac{-\sin \beta_K}{q_k} \\ -\mathrm{i} q_k \sin \beta_k & \cos \beta_k \end{bmatrix} \tag{3}$$

$$r_p = \frac{(M_{11} + M_{12} q_5) q_1 - (M_{21} + M_{22} q_5)}{(M_{11} + M_{12} q_5) q_1 + (M_{21} + M_{22} q_5)} \tag{4}$$

$$R_p = |r_p|^2 \tag{5}$$

The transformation of the sensing medium might change the resonance angle (Δθ), where S_{R1} = Δθ/Δn represents the sensitivity [44]. The BK7 glass has a low refractive index coupling prism to use in these biosensors. Figure 1 shows a conventional Kretschmann structure SPR biosensor that has a metallic layer to activate SPP. By applying a BK7 glass prism, the resulting Au metal layer SPR biosensor sensitivity is 133°/RIU, as shown in Figure 2. For a biochemical sensor, this sensitivity is unsatisfied [45]. Utilizing 2D materials TMDCs TaS_2, we have developed SPR biochemical sensors in the current paper to enhance the sensitivity of the sensors [46–48].

Figure 2a–e shows the changes of reflectivity versus the incident angle. The resonance angles of the TaS_2 sensor shift to higher incidence angles at one layer and the sensitive media refractive indices increase. Sensitivity can be increased by using 2D TMDCs material TaS_2-based biochemical sensors. Figure 2f shows the changes in sensitivity of TaS_2 on the Au surface. It shows that the biosensor sensitivity increases and then decreases with the addition of TaS_2 layers from 1 to 9; the highest sensitivity for TaS_2 biosensors is 201°/RIU when the TaS_2 layers accumulate to 8 layers. The most likely reason for the transformation is because the light utilization rate reduces with an increase in the number of TaS_2 layers. Therefore, the number of TaS_2 layers has an optimal value and cannot be increased unboundedly.
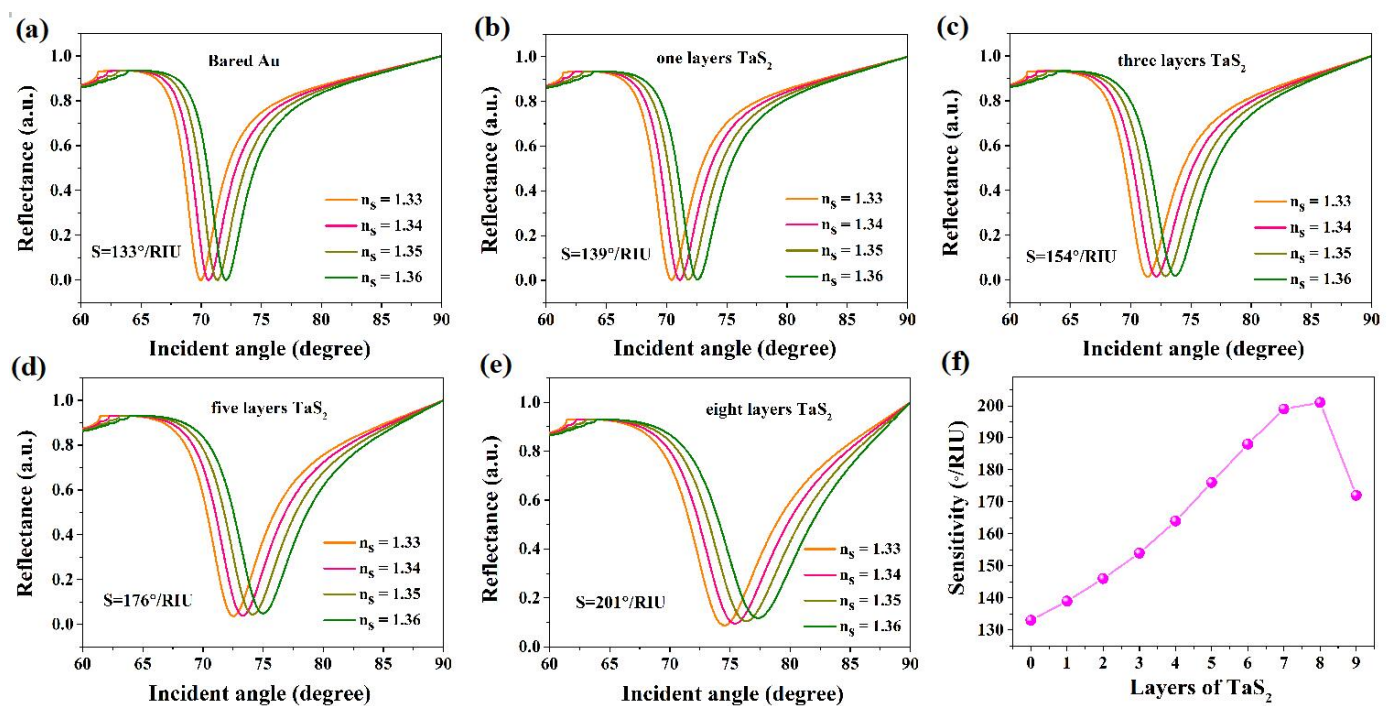
Figure 2. (**a**–**e**) Simulation change of reflectivity relative to incident angles with different numbers of TaS$_2$ nanosheets; (**f**) variation of sensitivity with respect to the number of TaS$_2$ nanosheets.

From Table 1, we can see that TaS$_2$-based Kretschmann structure SPR biosensors show an obviously improvement.

Table 1. Different 2D material sensing medium layers to improve biosensors.

2D Materials	Optimal Sensitivity	Maximum Sensitivity	Detection Limit	Ref.
Graphene oxide	91.1°/RIU	2715 nm/RIU	10^{-11} mol/L	[49,50]
MoS$_2$	49.2°/RIU	0.64 μA/ppb	11.52×10^{-3} ppb	[51,52]
MoSe$_2$	50.4°/RIU	2524 nm/RIU	3.5 nM	[53]
WS$_2$	48.6°/RIU	2459 nm/RIU	3.3 nM	[54]
TaS$_2$	201°/RIU	10.36°/μM	1 pM	Our work

3.2. Application of TaS$_2$ Based SPR Biosensors in Heavy Metal Ion Detection

The simulation results discussed in the last section provide details for depositing TaS$_2$ nanoparticles onto SPR chip surfaces. First, using layer-by-layer (LBL) techniques, we assembled the as-prepared TaS$_2$ nanosheets onto the SPR chip Au surface. Subsequently, using scanning electron microscopy (SEM), the surface morphology of TaS$_2$ nanosheets over the SPR chips was characterized, as shown in Figure 3. By increasing the dipping cycle, TaS$_2$ nanosheets were more thickly deposited, as shown in Figure 3a–c. Unexpectedly, it was observed that the morphology of the TaS$_2$ nanosheets was not affected by the LBL process, as can be seen in the right side of Figure 3a–c. Thus, assembly of TaS$_2$ nanosheets over SPR chip surfaces can be tuned by LBL assembly techniques. We have obtained SPR curves through different layers as the superstructure TaS$_2$ materials were assembled via LBL method.
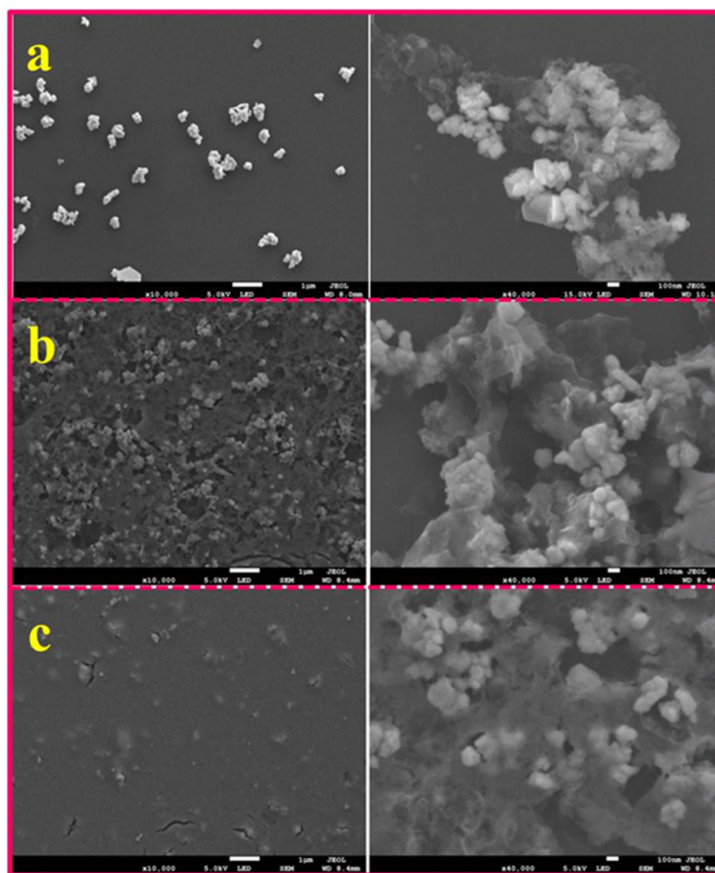
Figure 3. (**a**–**c**) The SEM images of the superstructure TaS$_2$ nanoparticles assembled with different thicknesses were obtained for 1 μm scale bar on the SPR chip surface. The panels on the right side are the magnified images, with a scale bar of 100 nm.

We have prepared SPR sensors with chips coated with TaS$_2$ nanosheets that, using SEM, can be seen to detect heavy metal ions. SPR spectra for different mercury ion concentrations from 10^{-12} M to 10^{-6} M were obtained, as shown in Figure 4a. We have identified the obvious shift curve toward higher resonance, which shows the Hg^{2+} adsorption onto the sensing layer material. The Hg^{2+} detection limit value in the calibration curve for the SPR angle shift versus Hg^{2+} concentration, from 10^{-12} M to 10^{-6} M Hg^{2+} solution concentration, 1 pM, were found to be the SPR sensor detection range [55]. This method's detection limit was 200 times lower compared with other techniques [56–58]. Figure 4b displays the SPR sensors calibration curve of angle shift along with mercury ion concentration without TaS$_2$ material, which is also in the range of 10^{-12}–10^{-6}, and the SPR spectra do not have much diversification. Figure 4c shows the incident angle changes for mercury ion concentrations from 10^{-12} M to 10^{-6} M; after linear fitting, we get a sensitivity of 10.36°/μM.

Apart from detecting Hg^{2+} in everyday drinking water, we also calculated the SPR sensor selectivity through investigating their responses to other heavy metal ions, for instance, Cr^{3+}, Cr^{6+}, Ag^{2+}, Pb^{2+}, Cu^{2+}, and Cd^{2+}. Under the same conditions, the response of the SPR sensors to dissimilar interfering ions at a level of 10^{-6} M concentration is shown in Figure 4d. In order to prevent the interference of an ion, we detected six different salts using the same concentration. The signal response Δθ of the six cations were similarly low, nearly 100 mdeg on the same 10^{-6} M concentrations. The results reveal that the SPR sensors have a strong selectivity to mercury ions compared with the other metal ions.
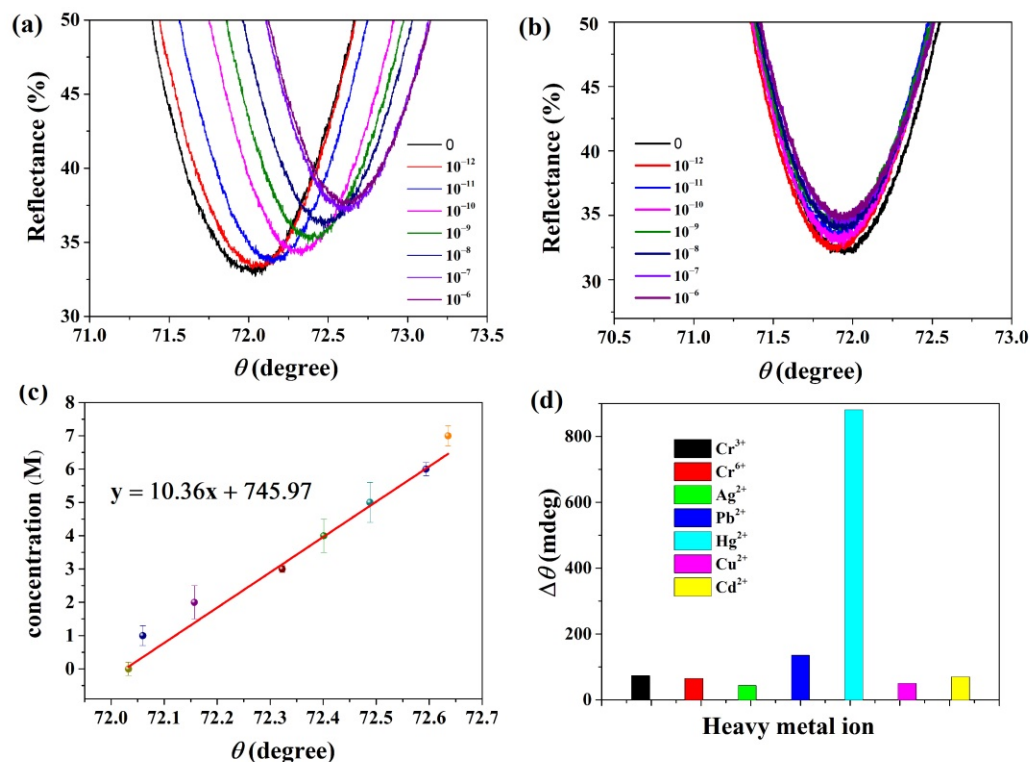
Figure 4. (**a**) The TaS$_2$ SPR spectra at different concentrations of Hg^{2+} from 10^{-12} to 10^{-6} M; (**b**) SPR spectra without TaS$_2$ at different concentrations of Hg^{2+} from 10^{-12} to 10^{-6} M; (**c**) the fitting curve of the incident angle at different concentrations of Hg^{2+} from 10^{-12} to 10^{-6} M; (**d**) selectivity of these TaS$_2$ based Hg^{2+} sensors.

3.3. Study of the Mechanism of High Sensitivity of These SPR Biosensors

The mechanism of the sensitivities of these TaS-based SPR sensors to detect Hg^{2+} was measured using elemental mapping of TaS$_2$ nanoflakes. Shown in the Figure 5, the elemental mapping characterizations of superstructure TaS$_2$ nanosheets by STEM EDS are displayed. Figure 5a shows a STEM image of TaS$_2$ nanoparticles; in the same way Figure 5b–d reveal Ta, S, and Ta + S EDS elemental maps. The distance between the layers of TaS$_2$ nanosheets is large, which is favourable for Hg^{2+} to enter the inner space where S atoms as binding sites are most likely located. These features allow the use of these TaS$_2$ nanosheets to detect Hg^{2+} in SPR sensors.

To get a clear picture of these highly sensitivity SPR sensors, we used the ESCALAB-250 instrument to measure X-ray photoelectron spectroscopy (XPS) in order to analyse the chemical states of Ta and S in structured TaS$_2$ nanoparticles and the original TaS$_2$ block. From Figure 6a, it is clear that two characteristic peaks of 167.1 eV and 168.4 eV are accredited to the 2p$^{2/3}$ and 2p$^{1/2}$ energy levels of divalent sulphide ions. Figure 6b, on the left side, illustrates that, at low intensity, the peak at 163.7 eV may be attributed to bridging S^{2-}, which represents unsaturated S atoms. The Ta 3d spectra of the TaS$_2$ powder are demonstrated by the peaks at 404.5 eV and 466.3 eV, corresponding to binding energies of Ta 4p$^{3/2}$ and Ta 4d$^{1/2}$, respectively (Figure 6a,b), which suggests the presence of TaS$_2$ structure 422.3 eV is the loss of Ta.

The left side of Figure 6b shows new peaks, which suggests the occurrence of the TaS$_2$ structure. The atomic configuration of TaS$_2$ is very dense on the surface of the substrate and also has a very high electronic conductivity, thus facilitating the combination of Hg^{2+}. In TaS$_2$ nanoflakes, the increased sensitivity of Hg^{2+} in the SPR sensor is promoted by the unsaturated S atoms.
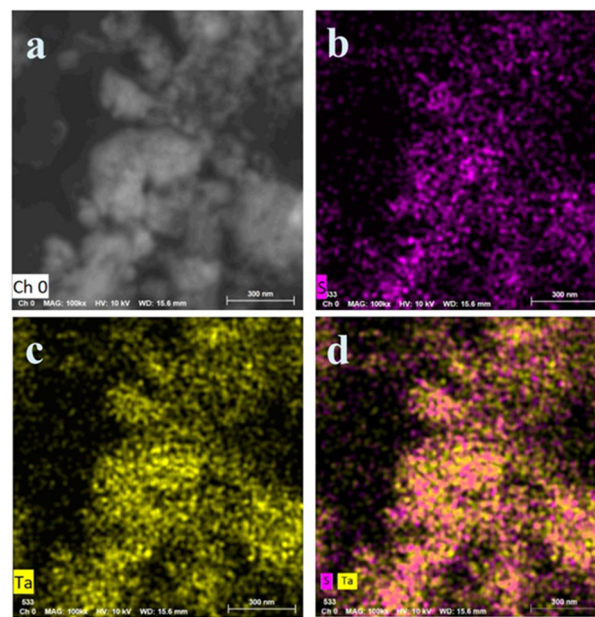
Figure 5. Elemental mapping characterizations of superstructure TaS_2 nanosheets by STEM EDS. (**a**) STEM image of TaS_2 nanosheets, similarly acquired with (**b–d**) Ta, S, and Ta + S EDS elemental maps.
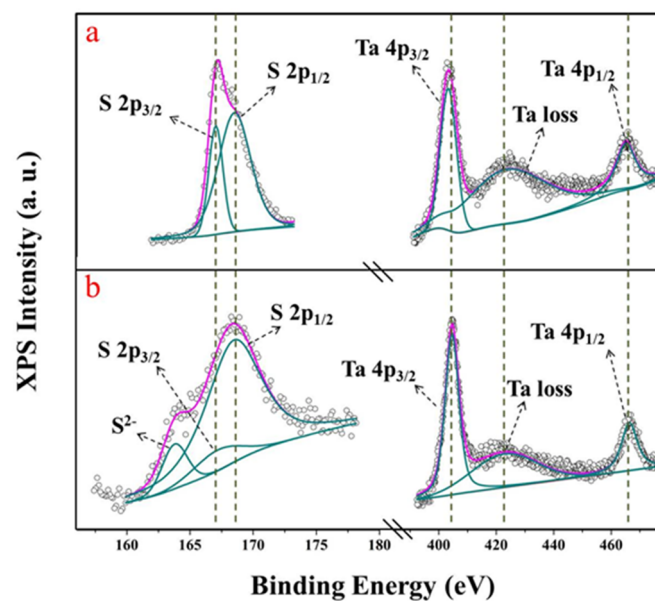

Figure 6. (**a**) XPS spectra of bulk TaS_2; (**b**) XPS spectra of TaS_2 nanoflakes.

4. Conclusions

Innovative SPR biochemical sensors using 2D TMDCs TaS_2 were designed and constructed to enhance the sensitivity to Hg^{2+} ions. The proposed design has improved the sensitivity of biochemical sensors to $201°/RIU$ for TaS_2. The SPR sensor was developed, and its performance was evaluated through a combination of simulation and experimental results. The detection sensitivity limit of TaS_2-based SPR biosensors is nearly 1 pM. TEM, HRTEM, and XPS were used to investigate the mechanism of these highly sensitive SPR sensors. From the obtained results, having a large inter-layer spacing and sufficient non-structural combination in the proposed TaS_2-based structure makes Hg^{2+} effectively transported and absorbed. These studies provide efficient methods for the detection of low Hg^{2+} concentrations and generalize the utilization of structured TaS_2 nanosheets.

References

1. Bolisetty, S.; Mezzenga, R. Amyloid-carbon hybrid membranes for universal water purification. *Nat. Nanotechnol.* **2016**, *11*, 365. [CrossRef]
2. Lamborg, C.H.; Hammerschmidt, C.R.; Bowman, K.L.; Swarr, G.J.; Munson, K.M.; Ohnemus, D.C.; Lam, P.J.; Heimbuerger, L.-E.; Rijkenberg, M.J.A.; Saito, M.A. A global ocean inventory of anthropogenic mercury based on water column measurements. *Nature* **2014**, *512*, 65. [CrossRef] [PubMed]
3. Gu, B.; Zhou, Y.; Zhang, X.; Liu, X.; Zhang, Y.; Marks, R.; Zhang, H.; Liu, X.; Zhang, Q. Thiazole derivative-modified upconversion nanoparticles for Hg^{2+} detection in living cells. *Nanoscale* **2016**, *8*, 276–282. [CrossRef]
4. Kosik-Bogacka, D.; Lanocha-Arendarczyk, N.; Kot, K.; Malinowski, W.; Szymanski, S.; Sipak-Szmigiel, O.; Pilarczyk, B.; Tomza-Marciniak, A.; Podlasinska, J.; Tomska, N.; et al. Concentrations of mercury (Hg) and selenium (Se) in afterbirth and their relations with various factors. *Environ. Geochem. Health* **2018**, *40*, 1683–1695. [CrossRef]
5. Mao, S.; Chang, J.; Pu, H.; Lu, G.; He, Q.; Zhang, H.; Chen, J. Two-dimensional nanomaterial-based field-effect transistors for chemical and biological sensing. *Chem. Soc. Rev.* **2017**, *46*, 6872–6904. [CrossRef] [PubMed]
6. Ai, K.; Ruan, C.; Shen, M.; Lu, L. MoS_2 Nanosheets with Widened Interlayer Spacing for High-Efficiency Removal of Mercury in Aquatic Systems. *Adv. Funct. Mater.* **2016**, *26*, 5542–5549. [CrossRef]
7. Geng, F.; Jiang, X.; Wang, Y.; Shao, C.; Wang, K.; Qu, P.; Xu, M. DNA-based dual fluorescence signals on and ratiometric mercury sensing in fetal calf serum with simultaneous excitation. *Sens. Actuators B Chem.* **2018**, *260*, 793–799. [CrossRef]
8. Huang, J.; Gao, X.; Jia, J.; Kim, J.-K.; Li, Z. Graphene Oxide-Based Amplified Fluorescent Biosensor for Hg^{2+} Detection through Hybridization Chain Reactions. *Anal. Chem.* **2014**, *86*, 3209–3215. [CrossRef] [PubMed]
9. Zhang, Z.; Tang, A.; Liao, S.; Chen, P.; Wu, Z.; Shen, G.; Yu, R. Oligonucleotide probes applied for sensitive enzyme-amplified electrochemical assay of mercury(II) ions. *Biosens. Bioelectron.* **2011**, *26*, 3320–3324. [CrossRef]
10. Kopysc, E.; Pyrzynska, K.; Garbos, S.; Bulska, E. Determination of mercury by cold-vapor atomic absorption spectrometry with preconcentration on a gold-trap. *Anal. Sci.* **2000**, *16*, 1309–1312. [CrossRef]
11. Karunasagar, D.; Arunachalam, J.; Gangadharan, S. Development of a 'collect and punch' cold vapour inductively coupled plasma mass spectrometric method for the direct determination of mercury at nanograms per litre levels. *J. Anal. At. Spectrom.* **1998**, *13*, 679–682. [CrossRef]
12. Elgazali, A.A.S.; Gajdosechova, Z.; Abbas, Z.; Lombi, E.; Scheckel, K.G.; Donner, E.; Fiedler, H.; Feldmann, J.; Krupp, E.M. Reactive gaseous mercury is generated from chloralkali factories resulting in extreme concentrations of mercury in hair of workers. *Sci. Rep.* **2018**, *8*, 3675. [CrossRef]
13. Kabashin, A.V.; Evans, P.; Pastkovsky, S.; Hendren, W.; Wurtz, G.A.; Atkinson, R.; Pollard, R.; Podolskiy, V.A.; Zayats, A.V. Plasmonic nanorod metamaterials for biosensing. *Nat. Mater.* **2009**, *8*, 867–871. [CrossRef]
14. Sreekanth, K.V.; Alapan, Y.; ElKabbash, M.; Ilker, E.; Hinczewski, M.; Gurkan, U.A.; de Luca, A.; Strangi, G. Extreme sensitivity biosensing platform based on hyperbolic metamaterials. *Nat. Mater.* **2016**, *15*, 621–627. [CrossRef]
15. Garoli, D.; Calandrini, E.; Giovannini, G.; Hubarevich, A.; Caligiuri, V.; de Angelis, F. Nanoporous gold metamaterials for high sensitivity plasmonic sensing. *Nanoscale Horiz.* **2019**, *4*, 1153–1157. [CrossRef]
16. Yan, R.; Wang, T.; Yue, X.; Wang, H.; Zhang, Y.-H.; Xu, P.; Wang, L.; Wang, Y.; Zhang, J. Highly sensitive plasmonic nanorod hyperbolic metamaterial biosensor. *Photon. Res.* **2022**, *10*, 84–95. [CrossRef]
17. Wei, Q.; Nagi, R.; Sadeghi, K.; Feng, S.; Yan, E.; Ki, S.J.; Caire, R.; Tseng, D.; Ozcan, A. Detection and Spatial Mapping of Mercury Contamination in Water Samples Using a Smart-Phone. *ACS Nano* **2014**, *8*, 1121–1129. [CrossRef] [PubMed]
18. Gu, W.; Pei, X.; Cheng, Y.; Zhang, C.; Zhang, J.; Yan, Y.; Ding, C.; Xian, Y. Black Phosphorus Quantum Dots as the Ratiometric Fluorescence Probe for Trace Mercury Ion Detection Based on Inner Filter Effect. *ACS Sens.* **2017**, *2*, 576–582. [CrossRef]
19. Berger, C.; Song, Z.; Li, X.; Wu, X.; Brown, N.; Naud, C.; Mayou, D.; Li, T.; Hass, J.; Marchenkov, A.N.; et al. Electronic confinement and coherence in patterned epitaxial graphene. *Science* **2006**, *312*, 1191–1196. [CrossRef]
20. Xue, T.; Cui, X.; Chen, J.; Liu, C.; Wang, Q.; Wang, H.; Zheng, W. A Switch of the Oxidation State of Graphene Oxide on a Surface Plasmon Resonance Chip. *ACS Appl. Mater. Interfaces* **2013**, *5*, 2096–2103. [CrossRef]

21. Han, S.-T.; Peng, H.; Sun, Q.; Venkatesh, S.; Chung, K.-S.; Lau, S.C.; Zhou, Y.; Roy, V.A.L. An Overview of the Development of Flexible Sensors. *Adv. Mater.* **2017**, *29*, 1700375. [CrossRef] [PubMed]
22. Xue, T.; Qi, K.; Hu, C. Novel SPR sensing platform based on superstructure MoS₂ nanosheets for ultrasensitive detection of mercury ion. *Sens. Actuators B Chem.* **2019**, *284*, 589–594. [CrossRef]
23. Yuting, Z.; Shuaiwen, G.; Leiming, W.; Jiaqi, Z.; Yuanjiang, X.; Xiaoyu, D. GeSe nanosheets modified surface plasmon resonance sensors for enhancing sensitivity. *Nanophotonics* **2020**, *9*, 327–336.
24. Xue, T.; Yu, S.; Zhang, X.; Zhang, X.; Wang, L.; Bao, Q.; Chen, C.; Zheng, W.; Cui, X. R6G molecule induced modulation of the optical properties of reduced graphene oxide nanosheets for use in ultrasensitive SPR sensing. *Sci. Rep.* **2016**, *6*, 21254. [CrossRef] [PubMed]
25. Loh, K.P.; Bao, Q.; Eda, G.; Chhowalla, M. Graphene oxide as a chemically tunable platform for optical applications. *Nat. Chem.* **2010**, *2*, 1015–1024. [CrossRef]
26. Tan, C.; Lai, Z.; Zhang, H. Ultrathin Two-Dimensional Multinary Layered Metal Chalcogenide Nanomaterials. *Adv. Mater.* **2017**, *29*, 1701392. [CrossRef]
27. Zhou, G.; Chang, J.; Pu, H.; Shi, K.; Mao, S.; Sui, X.; Ren, R.; Cui, S.; Chen, J. Ultrasensitive Mercury Ion Detection Using DNA-Functionalized Molybdenum Disulfide Nanosheet/Gold Nanoparticle Hybrid Field Effect Transistor Device. *ACS Sens.* **2016**, *1*, 295–302. [CrossRef]
28. Gooding, J.J.; Gaus, K. Single-Molecule Sensors: Challenges and Opportunities for Quantitative Analysis. *Angew. Chem. Int. Ed.* **2016**, *55*, 11354–11366. [CrossRef]
29. Li, H.; Tan, Y.; Liu, P.; Guo, C.; Luo, M.; Han, J.; Lin, T.; Huang, F.; Chen, M. Atomic-Sized Pores Enhanced Electrocatalysis of TaS2 Nanosheets for Hydrogen Evolution. *Adv. Mater.* **2016**, *28*, 8945–8949. [CrossRef]
30. Sanders, C.E.; Dendzik, M.; Ngankeu, A.S.; Eich, A.; Bruix, A.; Bianchi, M.; Miwa, J.A.; Hammer, B.; Khajetoorians, A.A.; Hofmann, P. Crystalline and electronic structure of single-layer TaS₂. *Phys. Rev. B* **2016**, *94*, 081404. [CrossRef]
31. Ma, L.; Ye, C.; Yu, Y.; Lu, X.F.; Niu, X.; Kim, S.; Feng, D.; Tomanek, D.; Son, Y.-W.; Chen, X.H.; et al. A metallic mosaic phase and the origin of Mott-insulating state in 1T-TaS₂. *Nat. Commun.* **2016**, *7*, 10956. [CrossRef] [PubMed]
32. Fu, W.; Chen, Y.; Lin, J.; Wang, X.; Zeng, Q.; Zhou, J.; Zheng, L.; Wang, H.; He, Y.; He, H.; et al. Controlled Synthesis of Atomically Thin 1T-TaS₂ for Tunable Charge Density Wave Phase Transitions. *Chem. Mater.* **2016**, *28*, 7613–7618. [CrossRef]
33. Yoshida, M.; Zhang, Y.; Ye, J.; Suzuki, R.; Imai, Y.; Kimura, S.; Fujiwara, A.; Iwasa, Y. Controlling charge-density-wave states in nano-thick crystals of 1T-TaS₂. *Sci. Rep.* **2014**, *4*, 7302. [CrossRef] [PubMed]
34. Ding, Y.; Wang, Y.; Ni, J.; Shi, L.; Shi, S.; Tang, W. First principles study of structural, vibrational and electronic properties of graphene-like MX₂ (M=Mo, Nb, W, Ta; X=S, Se, Te) monolayers. *Phys. B Condens. Matter* **2011**, *406*, 2254–2260. [CrossRef]
35. Yang, Y.; Fang, S.; Fatemi, V.; Ruhman, J.; Navarro-Moratalla, E.; Watanabe, K.; Taniguchi, T.; Kaxiras, E.; Jarillo-Herrero, P. Enhanced superconductivity upon weakening of charge density wave transport in 2H-TaS₂ in the two-dimensional limit. *Phys. Rev. B* **2018**, *98*, 035203. [CrossRef]
36. Wu, J.; Peng, J.; Yu, Z.; Zhou, Y.; Guo, Y.; Li, Z.; Lin, Y.; Ruan, K.; Wu, C.; Xie, Y. Acid-Assisted Exfoliation toward Metallic Sub-nanopore TaS₂ Monolayer with High Volumetric Capacitance. *J. Am. Chem. Soc.* **2018**, *140*, 493–498. [CrossRef]
37. Zeng, Z.; Tan, C.; Huang, X.; Bao, S.; Zhang, H. Growth of noble metal nanoparticles on single-layer TiS₂ and TaS2 nanosheets for hydrogen evolution reaction. *Energy Environ. Sci.* **2014**, *7*, 797–803. [CrossRef]
38. Zeng, S.; Hu, S.; Xia, J.; Anderson, T.; Dinh, X.-Q.; Meng, X.-M.; Coquet, P.; Yong, K.-T. Graphene-MoS₂ hybrid nanostructures enhanced surface plasmon resonance biosensors. *Sens. Actuators B Chem.* **2015**, *207*, 801–810. [CrossRef]
39. Polyanskiy, M.M. Refractive Index Database. Johnson and Christy 1972. Available online: http://refractiveindex.info (accessed on 4 April 2022).
40. Gupta, B.D.; Sharma, A.K. Sensitivity evaluation of a multi-layered surface plasmon resonance-based fiber optic sensor: A theoretical study. *Sens. Actuators B Chem.* **2005**, *107*, 40–46. [CrossRef]
41. Van Soest, J.P. Optical and Electronic Reflectivity of TaS2. 2018. Available online: https://hdl.handle.net/1887/64692 (accessed on 4 April 2022).
42. Albertini, O.R.; Liu, A.Y.; Calandra, M. Effect of electron doping on lattice instabilities in single-layer 1H-TaS₂. *Phys. Rev. B* **2017**, *95*, 235121. [CrossRef]
43. Hansen, W.N. Electric fields produced by propagation of plane coherent electromagnetic radiation in a stratified medium. *J. Opt. Soc. Am.* **1968**, *58*, 380–390. [CrossRef]
44. Maharana, P.K.; Jha, R. Chalcogenide prism and graphene multilayer based surface plasmon resonance affinity biosensor for high performance. *Sens. Actuators B Chem.* **2012**, *169*, 161–166. [CrossRef]
45. Zeng, S.; Baillargeat, D.; Ho, H.-P.; Yong, K.-T. Nanomaterials enhanced surface plasmon resonance for biological and chemical sensing applications. *Chem. Soc. Rev.* **2014**, *43*, 3426–3452. [CrossRef] [PubMed]
46. Qiao, Y.-B.; Li, Y.-L.; Zhong, G.-H.; Zeng, Z.; Qin, X.-Y. Anisotropic properties of TaS₂. *Chin. Phys.* **2007**, *16*, 3809–3814.
47. Reshak, A.H.; Auluck, S. Full-potential calculations of the electronic and optical properties for 1T and 2H phases of TaS₂ and TaSe₂. *Phys. B Condens. Matter* **2005**, *358*, 158–165. [CrossRef]
48. Sharma, S.; Auluck, S.; Khan, M.A. Optical properties of 1T and 2H phases of TaS₂ and TaSe₂. *Pramana* **2000**, *54*, 431–440. [CrossRef]

49. Meshginqalam, B.; Ahmadi, M.T.; Ismail, R.; Sabatyan, A. Graphene/Graphene Oxide-Based Ultrasensitive Surface Plasmon Resonance Biosensor. *Plasmonics* **2017**, *12*, 1991–1997. [CrossRef]

50. Choi, S.H.; Kim, Y.L.; Byun, K.M. Graphene-on-silver substrates for sensitive surface plasmon resonance imaging biosensors. *Opt. Express* **2011**, *19*, 458–466. [CrossRef]

51. Nigam, A.; Goel, N.; Bhat, T.N.; Rahman, M.T.; Dolmanan, S.B.; Qiao, Q.; Tripathy, S.; Kumar, M. Real time detection of Hg^{2+} ions using MoS_2 functionalized AlGaN/GaN high electron mobility transistor for water quality monitoring. *Sens. Actuators B Chem.* **2020**, *309*, 127832. [CrossRef]

52. Wu, L.; Zhu, J.; Gan, S.; Ma, Q.; Dai, X.; Xiang, Y. Application of Few-Layer Transition Metal Dichalcogenides to Detect the Refractive Index Variation in Lossy-Mode Resonance Sensors with High Figure of Merit. *IEEE Sens. J.* **2019**, *19*, 5030–5034. [CrossRef]

53. Zhu, J.; Ke, Y.; Dai, J.; You, Q.; Wu, L.; Li, J.; Guo, J.; Xiang, Y.; Dai, X. Topological insulator overlayer to enhance the sensitivity and detection limit of surface plasmon resonance sensor. *Nanophotonics* **2020**, *9*, 1941–1951. [CrossRef]

54. Zuo, X.; Zhang, H.; Zhu, Q.; Wang, W.; Feng, J.; Chen, X. A dual-color fluorescent biosensing platform based on WS_2 nanosheet for detection of Hg^{2+} and Ag^+. *Biosens. Bioelectron.* **2016**, *85*, 464–470. [CrossRef] [PubMed]

55. Thompson, M.; Ellison, S.L.R.; Wood, R. Harmonized guidelines for single-laboratory validation of methods of analysis—(IUPAC technical report). *Pure Appl. Chem.* **2002**, *74*, 835–855. [CrossRef]

56. Xuan, F.; Luo, X.; Hsing, I.M. Conformation-Dependent Exonuclease III Activity Mediated by Metal Ions Reshuffling on Thymine-Rich DNA Duplexes for an Ultrasensitive Electrochemical Method for Hg^{2+} Detection. *Anal. Chem.* **2013**, *85*, 4586–4593. [CrossRef] [PubMed]

57. Cui, L.; Wu, J.; Li, M.; Ju, H. Highly sensitive electrochemical detection of mercury (II) via single ion-induced three-way junction of DNA. *Electrochem. Commun* **2015**, *59*, 77–80. [CrossRef]

58. Shahat, A.; Elsalam, S.A.; Herrero-Martinez, J.M.; Simo-Alfonso, E.F.; Ramis-Ramos, G. Optical recognition and removal of Hg(II) using a new self-chemosensor based on a modified amino-functionalized Al-MOF. *Sens. Actuators B Chem.* **2017**, *253*, 164–172. [CrossRef]